PCCP

Accepted Manuscript

ROYAL SOCIETY OF CHEMISTRY

www.rsc.org/pccp

Journal Name

ARTICLE TYPE

Cite this: DOI: 10.1039/xxxxxxxxxx

Antiferromagnetic FeMn alloys electrodeposited from chloride-based electrolytes

Sandra Ruiz-Gómez[1], Rocío Ranchal[1], Manuel Abuín[1,2], Ana María Aragón[3], Víctor Velasco[1,3], Pilar Marín[1,3], Arantzazu Mascaraque [1,4] and Lucas Pérez[1,5]

Received Date
Accepted Date

DOI: 10.1039/xxxxxxxxxx

www.rsc.org/journalname

The capability of synthesizing Fe-based antiferromagnetic metal alloys would fuel the use of electrodeposition in the design of new magnetic devices such as high-aspect-ratio spin valves or new nanostructured hard magnetic composites. Here we report the synthesis of high quality antiferromagnetic FeMn alloys electrodeposited from chloride-based electrolytes. We have found that in order to grow homogeneous FeMn films it is necessary to incorporate a large concentration of NH_4Cl as additive in the electrolyte. The study of the structure and magnetic properties show that films with composition close to $Fe_{50}Mn_{50}$ are homogeneous antiferromagnetic alloys. We have established a parameter window for the synthesis of FeMn alloys that show antiferromagnetism at room temperature.

1 Introduction

In recent years the use of electrodeposition has proven to be a very useful technique for the synthesis of nanostructures in combination with e-beam lithography [1–3] or nanoporous templates [4,5]. In this sense, several examples have been reported in the field of magnetism related to the control of the magnetic properties of nanowires [6], the synthesis of core-shell structures [7] or to the measurement of weak antilocalization in the magnetotransport properties of single crystal individual nanowires [8]. However, the inability of growing electrodeposited antiferromagnetic materials limits the use of this growth technique in other research areas in which its use would be potentially relevant. In particular, two main areas will profit from the electrodeposition of metal antiferromagnets: spin-electronics and the search of rare-earth-free magnets.

The discovery of giant magnetoresistance and the subsequent development of spin valves represented a revolution in magnetic storage technology in the 90's, given rise to the born of spintronics. The use of nanowires to fabricate *race track memories* is one of the most active fields of current research within this area [9–11]. The operation of these devices requires the inclusion of spin-valves in the structures, devices that need an antiferromagnetic material to fix one of the ferromagnetic layers forming the structure [12]. The use of electrodeposition to fabricate spin valves has several technological advantages like the growth of multiple spin valves in a single nanowire and the study of the collective behavior of them. It would also allow to grow vertical devices with high aspect ratio. However, to date, only electrodeposited synthetic antiferromagnets have been used in these structures [13,14] due to the difficulty in electrodepositing antiferromagnetic metals. To our knowledge, there has only been one report in which an antiferromagnetic electrodeposited metal (FeMn) is used in a spin-valve although no information about the growth or the magnetic properties is reported [15].

The search of rare-earth-free permanent magnets [16,17], is another research fields with great potential in current magnetism. The electrodeposition of antiferromagnetic nanomaterials can also provide interesting solutions to this problem: the coupling between ferromagnetic and antiferromagnetic iron based materials at the nanometer scale would combine the high saturation magnetization of the Fe and the interfacial exchange coupling between the two materials, producing a magnetically hard composite [18,19]. Therefore, the possibility of electrodepositing Fe-based antiferromagnetic material provides this technology with a new ingredient to fabricate new Fe-based permanent magnets.

Manganese layers can be grown from sulphate based electrolytes [20–22] but larger crystals are obtained when using chlorides [23]. The electrodeposition of Mn-based alloys have been already reported, as SeMn [24] from sulphates or ZnMn [25] and BiMn [26] from chlorides. The main goal of this paper is to electrodeposite high quality Fe_xMn_{1-x} thin films from aqueous media, in the search for an antiferromagnetic electrodeposited metal

[1] *Dept. Física de Materiales. Universidad Complutense de Madrid. 28040 Madrid, Spain.*
[2] *CEI Campus Moncloa, UCM-UPM, 28040 Madrid, Spain*
[3] *Instituto de Magnetismo Aplicado. ADIF-UCM. PO Box 155, E-28230 Las Rozas, Spain.*
[4] *Unidad Asociada IQFR (CSIC)-UCM, Madrid, 28040, Spain*
[5] *Instituto de Sistemas Optoelectrónicos y Microtecnología. Universidad Politécnica de Madrid. 28040 Madrid, Spain*

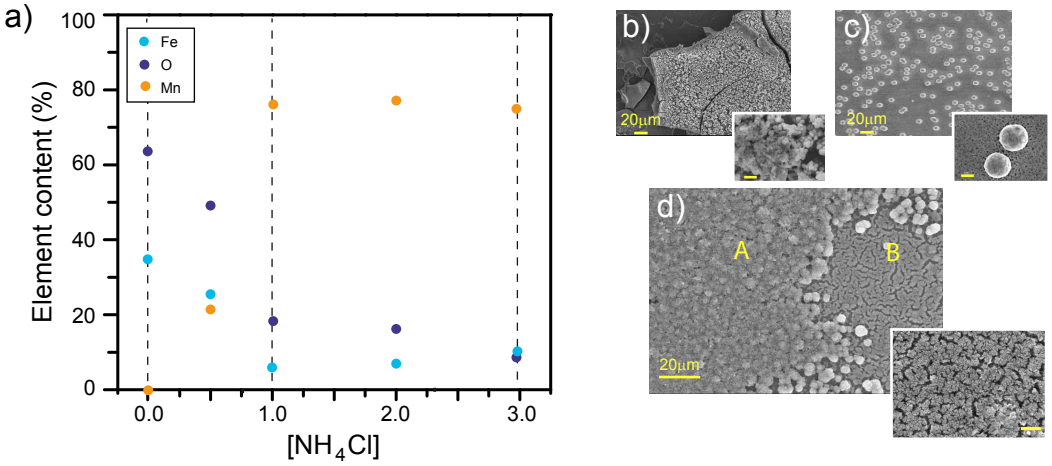

Fig. 1 Study of thin films grown with different NH_4Cl concentration in the electrolyte. (a) Concentration of the different elements (Fe, Mn and O) as a function of the NH_4Cl concentration in the electrolyte. SEM images of thin films grown (b) without NH_4Cl, (c) with 1 M NH_4Cl and (d) with 3 M NH_4Cl in the electrolyte. To show the morphology of the layers more clearly, the three SEM images are accompanied by an inset with larger magnification, in which the yellow bar corresponds to 1μm.

layer.

2 Experimental

FeMn films have been electrodeposited on Si/Ta/Au substrates by potentiostatic deposition using a Ecochemie Autolab PGSTAT potentiostat/galvanostat, which was also used for the electrochemical characterization. The different electrolytes used in this work contained $MnCl_2$ (0.4 M) as Mn^{2+} source, $FeCl_2$ (from 4 mM to 400 mM) as Fe^{2+} source and NH_4Cl (up to 3 M) as additive. pH was adjusted to 3 dropping H_2SO_4 to the solution. Unless otherwise stated, the electrolyte was deaerated for one hour before electrodeposition using N_2. Electrodeposition was carried out at room temperature, under stirring, in a three-electrode configuration, using a Pt gauze as counter electrode and a Ag/AgCl reference electrode (BASi). All samples were electrodeposited during 40 s under a growth potential of -1.7 V (vs. Ag/AgCl). Under these conditions, all grown samples have an average thickness of 70 nm. To avoid the possible degradation of the electrolyte due to the oxidation of Fe^{2+} ions into Fe^{3+} ions, fresh electrolyte was prepared and used for each experiment and growth.

A Scanning Electron Microscope (SEM) JEOL JEM 6335 equipped with Energy Dispersive X-Ray Microanalysis was used to study the morphology and composition of the samples. All the EDX measurements are expressed in unit of % at. The crystalline structure was studied by grazing incident X-ray diffraction (XRD) with PANalytical X-ray diffractometers using Cu K_α radiation. X-ray absorption experiments were performed at the SpLine beamline at the European Synchrotron Radiation Facility (ESRF). We carried out X-ray absorption near edge structure (XANES) spectroscopy experiments at the Fe K-edge (7.11 keV) and Mn K-edge (6.539 keV) in fluorescence mode at room temperature.

We have measured hysteresis loops as well as thermal evolution of magnetization below and above room temperature. Magnetic measurements at room and low temperature (5-300 K) were performed in a Superconducting Quantum Interference Device (SQUID) and in a Vibrating Sample Magnetometer (VSM), both from Quantum Design. Thermal evolution of magnetization below room temperature was measured under an applied field of 500 Oe either under field-cooling (FC) and zero-field cooling (ZFC) conditions. A 20 kOe magnetic field was applied before the measurement of the FC curve. Thermal evolution of magnetization at high temperature (300-460 K)was measured in a LakeShore VSM Magnetometer with an applied field of 5 kOe.

3 Results and discussion

3.1 Electrodeposition of Fe_xMn_{1-x} alloys

The electrodeposition of metal manganese is quite complex due to its low reduction potential, beyond the hydrogen and water reduction potentials. To incorporate Mn to the films, it is necessary to stabilize the Mn^{2+} ion in the electrolyte. For this purpose, their complexation using Cl^- has been proved to be essential[26]. The NH_4^+ ion has also a beneficial effect in Mn electrodeposition: it increases the solution conductivity and prevents the precipitation of manganese oxides and hydroxides[22]. We have added NH_4Cl as additive to take advantage of these effects.

To check the effect of the concentration of NH_4Cl, we have electrodeposited a series of samples varying the concentration of NH_4Cl from 0 to 3 M in an electrolyte containing 0.4 M $MnCl_2$ and 4 mM $FeCl_2$. In these experiments, the electrolyte was not deaerated before or during the electrodeposition process or the electrochemical measurements. Figure 1.a clearly shows that the incorporation of Mn in the layers is extremely dependent on the NH_4Cl content in the electrolyte. In fact, if no additive is present, there is not measurable incorporation of Mn in these layers while the relative Mn content in the layer increases up to 80% when increasing the additive concentration. The oxygen content of the sample also depends on the NH_4Cl content. Although the measurement of O using EDX is semiquantitative, the large obtained values indicate the presence of an important amount of oxides in the grown layers, which is reduced down to 10% by incorporating

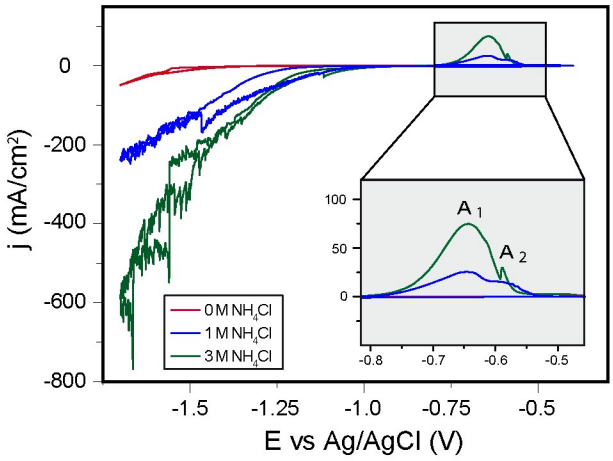

Fig. 2 Cyclic voltammograms measured in the electrolytes used for the growth of the films reported in Figure 1. The inset are enlargements of the anodic branch of the curves.

the additive.

Although the concentration of Mn is determinant to have antiferromagnetic behavior, the morphology of the grown layer is fundamental for real applications. The morphology also depends on the NH_4Cl content. In particular, the presence of NH_4Cl is essential to accomplish adherent layers. Otherwise, the layers are full of cracks and separate from the substrate after growth (Figure 1.b). For low NH_4Cl concentration, Mn incorporates to the layer as segregated micrometer-size clusters in an Fe layer (measured by EDX). This can be observed in Figure 1.c. Only when the concentration of NH_4Cl excedes 2 M, compacted samples are produced. In some cases, areas with different composition and morphology are detected (Figure 1.d): zone A, rougher, with a composition $Fe_9Mn_{68}O_{23}$ and zone B, more compacted, with a composition $Fe_{23}Mn_9O_{68}$ inferred by EDX. In this case, the sample is nanocrystalline, with crystal size of a few nanometers.

We extract similar conclusions from the electrochemical measurements reported. In Figure 2 we show cyclic voltammograms measured in electrolytes with different NH_4Cl. In the electrolyte without additive (red line), no dissolution of Mn is detected in the anodic branch of the voltammogram. This is clearly related to the low adhesion of the layers in this case: after deposition, the Mn layer separates from the substrate and no anodic dissolution is possible. When adding NH_4Cl (blue line), an anodic peak is observed, peak whose amplitude increases when increasing the concentration of additive (green line). A detail of the anodic branch (inset of Figure 2) shows two peaks in this area, named A_1 and A_2. The presence of these two peaks have been already reported by Benfedda *et al.*[26] in the BiMn system, relating A_1 with Mn dissolution and A_2 with the presence of oxides and/or hydroxides. The A_2/A_1 ratio decreases when the NH_4Cl concentration increases, which coincides with the decreasing of the oxygen content shown in Figure 1.a. Therefore, the presence of this second peak in the voltammograms is a fingerprint of the presence of Mn oxides and/or hydroxides in the layers. After analyzing the role of NH_4Cl we have fixed the NH_4Cl concentration in 3 M.

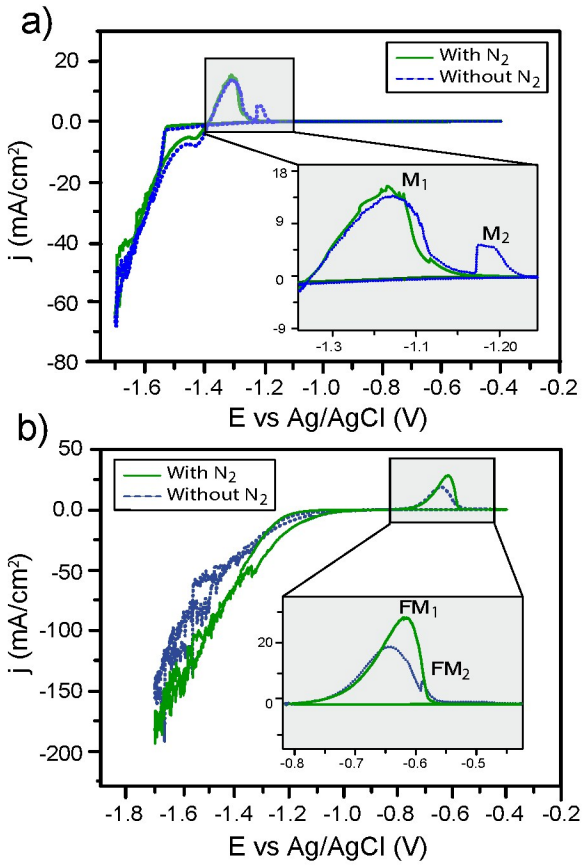

Fig. 3 Cyclic voltammograms measured in electrolytes containing (a) Mn^{2+} and (b) both Mn^{2+} Fe^{2+} ions. The inset are enlargements of the anodic branch of the curves to make easier the comparison between the curves measured with and without deareation.

Although the oxygen content in the layers is considerably reduced by increasing the NH_4Cl up to 3 M, it is necessary to decrease it further. For this purpose, the electrolyte was deaerated with N_2 for one hour before electrodeposition to reduce the O_2 dissolved. The N_2 flow was also maintained during the electrodeposition process. Figure 3 compares cyclic voltamograms measured in electrolytes with and without deaeration. The curves in Figure 3.a have been measured in electrolytes containing only Mn^{2+} ions whereas the electrolytes used in the measurements shown in Figure 3.b contained both Mn^{2+} and Fe^{2+} ions. After deaeration, peaks M_2 and FM_2 disappears and only one peak appears in the anodic branch of each curve (M_1 and FM_1) which means that the oxygen content is further reduced. In fact, the oxygen content is beyond the detection limit of EDX for layers grown under these conditions. In addition, morphology also improves with deaeration. Compared with the layers without deaeration, the FeMn layers grown after deaeration of the electrolyte are more homogeneous in both, roughness and composition. In fact, no differences in composition have been found measuring EDX in ten different places of each film.

Finally, it is important to control the Fe content in the layers, in order to have the appropriate magnetic properties. We have varied two orders of magnitude the $FeCl_2$ concentration in the elec-

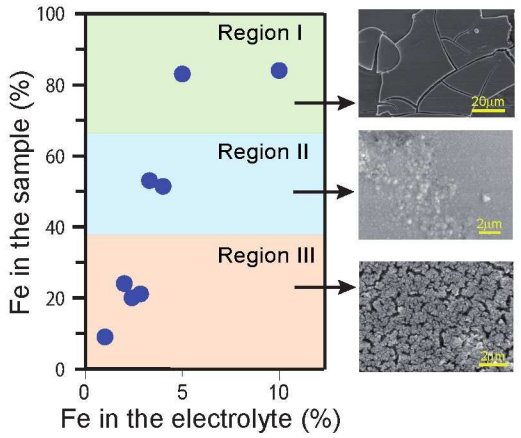

Fig. 4 Variation of the Fe content in the films as a function of the concentration of Fe^{2+} in the electrolyte. SEM images on the right are representative of the morphology of the films belonging to the three zones marked with different colors in the graph.

trolyte, from 4 mM to 400mM, keeping constant both the $MnCl_2$ and the NH_4Cl concentration. Figure 4 represents the relative Fe content in the sample as a function of the relative concentration of Fe^{2+} in the electrolyte (in molar fraction), defined as follows:

$$\text{Fe in the sample} = 100 \times \frac{[\text{Fe}]}{[\text{Fe}] + [\text{Mn}]} \quad (1)$$

$$\%\text{Fe in the electrolyte} = 100 \times \frac{[\text{Fe}^{2+}]}{[\text{Fe}^{2+}] + [\text{Mn}^{2+}]} \quad (2)$$

Two interesting features can be observed in the composition and morphology of the samples as a function of the $FeCl_2$ content. First of all, there is a strong variation of the Fe content in the sample, from 10% to 90% when the relative Fe^{2+} concentration in the electrolyte varies from 2% to 8%. This provides a narrow window to control the composition of these alloys. Second, the change in composition is associated with a change in the morphology of the thin films. We can define three different regimes. When growing in the Fe-rich region (region I) the layers are non-adherent and present a cracked surface. In the opposite region (region III), Mn-rich samples are homogeneous and adherent, but have large roughness. Finally, films with composition close to $Fe_{50}Mn_{50}$ (region II) are homogeneous and less rough.

3.2 Crystalline structure

The crystalline structure of three different samples, a pure Mn sample, a Mn-rich sample and a $Fe_{50}Mn_{50}$ sample have been studied by XRD and the diffractograms are shown in figure 5. It is important to point out that, due to the grazing incident configuration, the measurements are particularly sensitive to surface oxidation. In fact, the broad peak observed around $2\theta = 55^{o}$, that it is present in all the layers, has its origin in surface oxides. Apart from this, all the grown layers are crystalline. In the pure Mn layer (red line), reflections corresponding to α−Mn and different manganese oxides (Mn_3O_4 and MnO_2) can be observed. The Mn-rich layer shows reflections corresponding to manganese

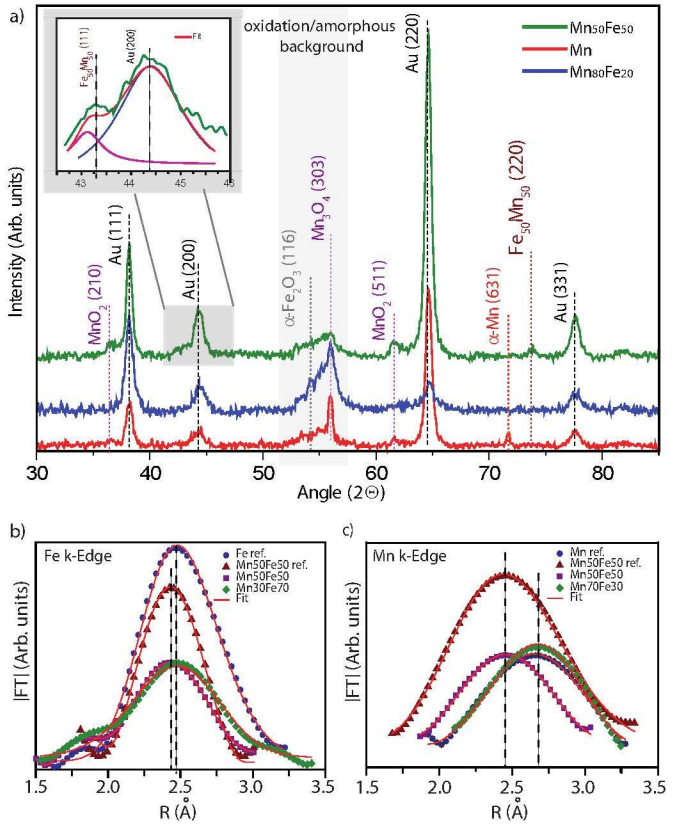

Fig. 5 (a) XRD diffraction pattern of a pure Mn layer and a Mn-rich and a $Mn_{50}Fe_{50}$ electrodeposited layers. The inset shows the deconvolution of the peak marked with the shadow square. (b) Fourier transform of the Fe K-edge and (c) Mn K-edge of the XANES signals measured in grown as well as reference samples. Red lines correspond to the fitting to a Lorentzian curve.

(Mn_3O_4) and iron (α−Fe_2O_3) oxides. Therefore, the Mn-rich samples are oxidized and do not shown any peak corresponding to the $Fe_{50}Mn_{50}$ structure.

In the layer grown in region II, with composition close to $Fe_{50}Mn_{50}$, we observe diffraction peaks related to the Fe-Mn antiferromagnetic alloy structure. In particular, we observe the two more intense reflection of this structure, according to the JCPDS card 04-002-0987: the (111) reflection, after a deconvolution of the peak around $2\theta = 43.1^{o}$ and the (220) reflection around $2\theta = 50.2^{o}$. This is a clear indication that the $Fe_{50}Mn_{50}$ phase has been formed in this layer. No reflections from pure Mn or Fe can be observed. Moreover, this layer does not shown peaks corresponding to manganese or iron oxides, as well as pure Mn or Fe, and therefore, it is clearly less oxidized.

In order to have a deeper insight in the structure, we have performed XAS measurements in three electrodeposited layers with composition $Mn_{50}Fe_{50}$, $Mn_{30}Fe_{70}$ and $Mn_{70}Fe_{30}$. We have also measured pure Fe and Mn foils as well as a $Mn_{50}Fe_{50}$ foil as a reference. Figure 5.b shows the Fourier transform (FT) of the XANES data measured in the Fe K-edge. As the position of the peaks give information about the bond lengths, the comparison between the electrodeposited and reference samples (the Fe, Mn and $Mn_{50}Fe_{50}$ foils) provides us with additional information about the structure

of the layers. The position of the peak for the Fe-rich sample coincides with the position for the Fe reference foil, indicating the presence of Fe clusters in the sample. In the $Mn_{50}Fe_{50}$ sample, the peak is shifted towards lower R values, as well as in the reference $Mn_{50}Fe_{50}$ foil. A similar behavior is observed when measuring close to the Mn K-edge (see Figure 5.c). The position of the peak for the Mn-rich sample coincides with the position for the Mn reference foil, showing the presence of segregated Mn clusters in the sample. Finally, in the case of the $Mn_{50}Fe_{50}$ electrodeposited sample, the peak position coincides with the one of the reference $Mn_{50}Fe_{50}$ foil. Thus the analysis of the XANES data confirms the formation of the alloy in the case of the $Mn_{50}Fe_{50}$ films.

3.3 Magnetic properties

We have studied the magnetic properties of samples grown in region III (Mn-rich samples) and region II ($Fe_{50}Mn_{50}$ samples. To understand the magnetic behavior of the different layers, it is important to note that Mn is an allotropic material which have four phases, three paramagnetic and one antiferromagnetic with Néel temperature close to 96 K.[27] In MnFe alloys, the Néel temperature increases with the increment of the Fe content, being antiferromagnetic at room temperature for Fe:Mn ratios close to 1:1[28].

Figure 6.a shows representative FC-ZFC curves of samples with less than 50% Fe (region III in Figure 4.a). In particular, we show the curves corresponding to films with composition $Fe_{10}Mn_{90}$ and $Fe_{30}Mn_{70}$. Two features are clearly observed in these curves. First, there is a clear a transition at around 100 K, transition which is more clearly shown in the derivative of the ZFC curve (Figure 6.a). Secondly, ZFC and FC curves do not match above the transition temperature, which proves the existence of magnetic order above this temperature. These features can be can be explained considering that, in these two samples, the Fe and Mn in the sample growth segregated and, therefore, the layers are composed by Mn clusters inside an Fe-rich matrix. The transition at around 100 K is shown at the same temperature for the samples independently of the composition. This transition corresponds to the Neel transition in pure Mn clusters. The separation between FC and ZFC curves above the transition, which is fingerprint of a ferromagnetic component, is due to the Fe-rich matrix, which is expected to be ferromagnetic well above room temperature.

This segregation in the Mn-rich samples is also confirmed by measuring the hysteresis loops of the layers. Figure 7 show the hysteresis loops of a $Fe_{30}Mn_{70}$ film measured at room temperature and also at low temperature (5 K) after cooling the sample in a 20 kOe magnetic field. The inset is an enlargement of the central part of the loops. In the measurement at low temperature there is a clear ferromagnetic component together with a shift of the hysteresis loop in the direction of the cooling magnetic field, a clear indication of the existence of exchange bias. This shift disappears when measuring at room temperature. Again, this magnetic behavior can be explained assuming an Fe-rich matrix, responsible of the ferromagnetic signal, coupled with antiferromagnetic Mn clusters. The coupling between the ferromagnetic Fe and the antiferromagnetic Mn is the origin of the observed exchange bias, phenomenon that disappears above the Neel temperature of the

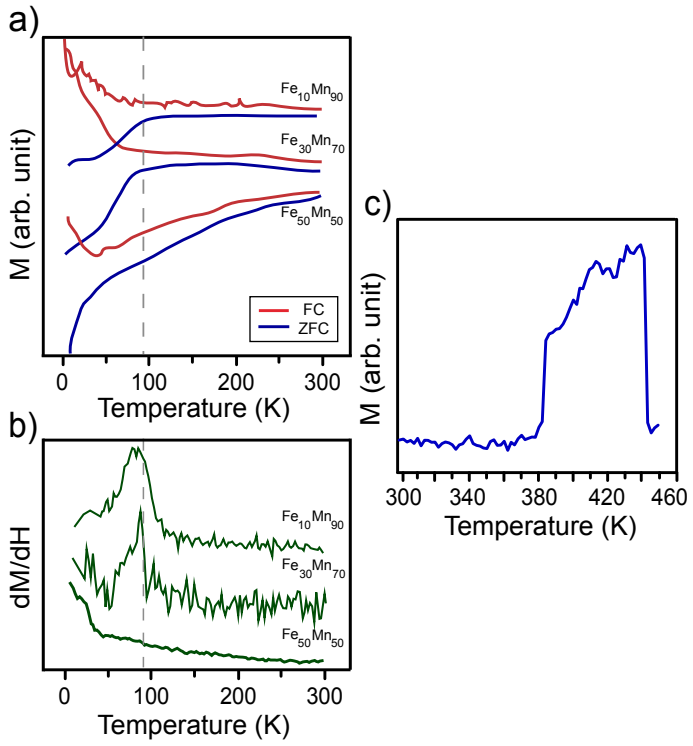

Fig. 6 (a) Thermal evolution of magnetization (FC-ZFC curves) and (b) derivative of the ZFC curves for samples grown in the region III of figure 4.a. The Néel temperature of pure Mn is indicated in the figure as a dashed line. (c) Thermal evolution of magnetization measured at high (300-460 K) temperature for samples with composition $Fe_{50}Mn_{50}$.

antiferromagnetic Mn. Therefore, the exchange bias is not observed in the hysteresis loop measured at room temperature.

The magnetic behavior of the sample with composition close to $Fe_{50}Mn_{50}$ (region II) is completely different. In particular, the previously observed transition at 100 K disappears, (see Figure 6.a) which suggests that this transition is shifted towards higher temperature. The absence of the transition at 100 K for this particular sample is again more clear in Figure 6.b, in which the derivative of the ZFC curve for the three samples is graphed. Whereas there is a clear peak in the derivative for the $Fe_{10}Mn_{90}$ and $Fe_{30}Mn_{70}$ samples, as mentioned before, no peak is observed for the $Fe_{50}Mn_{50}$ layer. In addition, the thermal evolution of magnetization at high temperature (Figure 6.d) show a transition at 450 K, very near to the reported value of Néel temperature of a $Fe_{50}Mn_{50}$ alloy[29]. This is a strong indication that in this case we have an antiferromagnetic alloy with transition temperature above room temperature and not segregation of Mn in the the film. It should be noted that the evolution of magnetization at high temperature has been measured at a quite large applied field to have enough signal in the magnetometer. This field is the origin of the increase of magnetization observed when approaching the transition temperature. Close to this temperature, the exchange coupling in the antiferromagnetic alloy is weakened, favoring the alignment of the magnetic moments along the direction of the applied field.

The analysis of magnetic measurements confirm what was expected from the structural characterization: the electrodeposited

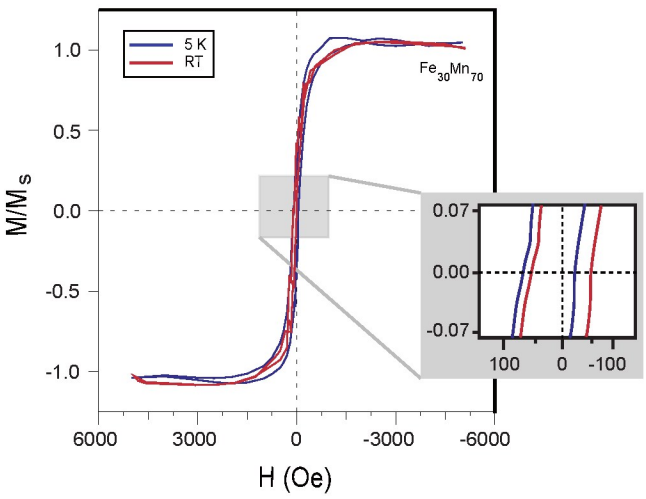

Fig. 7 Hysteresis loop measured in a $Fe_{30}Mn_{70}$ film at low (5 K) and room temperature. The inset is an enlargement of the central part of the loop to show the exchange bias phenomena in the loop measured at low temperature

films with composition close to $Fe_{50}Mn_{50}$ are antiferromagnetic alloys with Néel transition above room temperature.

4 Conclusions

We have successfully defined a experimental parameter window to grow FeMn antiferromagnetic alloys using electrochemical deposition. A large concentration of NH_4Cl is needed to allow Mn to incorporate in the layers. The concentration of Fe in the films strongly depends on the relative concentration of Fe^{2+} in the electrolyte and varying the concentration of Fe^{2+} from 1 % to 9 %, it is possible to sweep the entire range of Fe_xMn_{1-x} alloys compositions in the sample. Regarding Mn content, we have identified three different regions. For low Mn content, the films are non-adherent. The films with high Mn content are very rough, with Mn and Fe rich segregated areas. On the contrary, samples with composition close to $Fe_{50}Mn_{50}$ are homogeneous in both composition and roughness . These samples also show a clear antiferromagnetic behavior at room temperature. These results open the path for electrodepositing nanodevices which require an antiferromagnetic material in its structure.

Acknowledgments

This paper is dedicated to the memory of our colleague, Dr. Patricia Crespo, who recently passed away. This work was funded by MINECO under projects MAT2011-28751-C02-02 and MAT2014-52477-C5-2-P. We thank the Spanish National Center of Electron Microscopy for SEM measurements and SPLINE beamline staff at the ESRF for their help during the XAS experiments. Manuel Abuín acknowledges the UCM Campus de Excelencia Internacional (PICATA Program).

References

1 Y. Yang, S. C. Kung, D. K. Taggart, C. Xiang, F. Yang, M. A. Brown, A. G. Guell, T. J. Kruse, J. C. Hemminger and R. M. Penner, *Nano Lett*, 2008, **8**, 2447–2451.

2 E. J. Menke, M. A. Thompson, C. Xiang, L. C. Yang and R. M. Penner, *Nat. Mater.*, 2006, **5**, 914–919.

3 S. Gosh, J. E. Hujdic, A. Villicana-Bedolla and E. J. Menke, *J. Phys Chem. C*, 2011, **36**, 115.

4 C. E. Carreon-Gonzalez, J. de la Torre, L. Piraux and A. Encinas, *Nano Lett*, 2011, **11**, 2023–2027.

5 C. T. Sousa, D. C. Leitao, M. P. Proenca, J. Ventura, A. M. Pereira and J. P. Araujo, *Appl. Phys. Rev.*, 2014, **1**, 031102.

6 L. Sun, Y. Hao, C. L. Chien and P. C. Searson, *IBM J. Res. & Dev.*, 2005, **49**, 79–102.

7 D. Shi, J. Chen, S. Riaz, W. Zhou and X. Han, *Nanotechnology*, 2012, **3**,.

8 N. Marcano, S. Sangiao, M. Plaza, L. Perez, A. Fernandez-Pacheco, R. Cordoba, M. C. Sanchez, L. Morellon, M. Ibarra and J. M. de Teresa, *App. Phys. Lett*, 2010, **96**, 8.

9 S. S. P. Parkin, M. Hayashi and L. Thomas, *Science*, 2008, **320**, 190–194.

10 S. S. P. Parkin, M. Hayashi and L. Thomas, *Nat. Nanotechnol.*, 2013, **8**, 411–416.

11 J. H. Franken, H. J. M. Swagten and B. Koopmans, *Nat. Nanotechnol.*, 2012, **7**, 499–503.

12 B. Dieny, V. S. Speriosu, S. S. P. Parkin, B. A. Gurney, D. R. Wilhoit and D. Mauri, *Phys. Rev. B*, 1991, **43**, 1297–1300.

13 K. Attenborough, H. Boeve, J. D. Boeck, G. Borghs and J. P. Celis, *Appl. Phys. Lett*, 1999, **74**, 2206.

14 H. Yu, S. Granville, D. P. Yu and J. P. Ansermet, *Phys. Rev. Lett*, 2010, **104**,.

15 H. Wang, Y. Wu, Q. Li, M. Wang, G. Li and L. Zhang, *Appl. Phys. Lett.*, 2006, **89**, 052107.

16 N. Jones, *Nature*, 2011, **472**, 22–23.

17 J. M. D. Coey, *IEEE Trans. Magn.*, 2011, **47**, 4671–4681.

18 B. Balamurugan, D. J. Sellmyer, G. Hadjipanayis and R. Skomski, *Scripta Materialia*, 2012, **67**, 542.

19 C. Feng, B. Li, J. Teng, Y. Jiang and G. Yu, *Thin Solids Films*, 2009, **517**, 2745–2748.

20 J. Gong and G. Zangari, *Appl. Phys. Lett.*, 2002, **149**, C209–C217.

21 P. Wei, O. E. Hileman, M. Reza-Bateni, X. Deng and A. Petric, *Surf. and Coat. Technol.*, 2007, **201**, 7730–7745.

22 J. Lu, D. Dreisinger and T. Gluck, *Hydrotermallurgy*, 2014, **141**, 105–116.

23 A. Sulcius, E. Griskonis, K. Kantminiene and N. Zmuidzinaviciene, *Hydrometallurgy*, 2013, **137**, 33–37.

24 T. Mahalingam, S. Thanikaikarasan, V. Dhanasekaran, A. Kathalingam, S. Velumani and J. K. Rhee, *Mater. Sci. Eng. B*, 2010, **174**, 257–262.

25 P. Dáz-Arista, Z. I. Ortiz, H. Ruiz, R. Ortega, Y. Meas and G. Trejo, *Surf. Coat. Technol.*, 2009, **203**, 1167–1175.

26 B. Benfedda, N. Benbrahim, A. Kadri, E. Chainet, F. Charlot and S. Coindeau, *Electrochim. Acta*, 2011, **56**, 1275–1282.

27 U. El-Hanany and W. W. Warren Jr., *Phys. Rev. B*, 1975, **12**, 861–876.

28 W. Williams Jr. and J. L. Stanford, *Phys. Rev. B.*, 1973, **7**,

3244–3250.
29 C. Won, Y. Z. Wu, H. W. Zhao, A. Scholl, A. Doran, W. Kim, T. L. Owens, X. F. Jin and Z. Q. Qiu, *Phys. Rev. B*, 2005, **71**, 024406.